SCIENTIFIC REPORTS

Enhanced optical absorption via cation doping hybrid lead iodine perovskites

Zhen-Kun Tang[1,2], Zhi-Feng Xu[1], Deng-Yu Zhang[1], Shu-Xian Hu[2], Woon-Ming Lau[2,3] & Li-Min Liu[2]

The suitable band structure is vital for perovskite solar cells, which greatly affect the high photoelectric conversion efficiency. Cation substitution is an effective approach to tune the electric structure, carrier concentration, and optical absorption of hybrid lead iodine perovskites. In this work, the electronic structures and optical properties of cation (Bi, Sn, and Tl) doped tetragonal formamidinium lead iodine $CH(NH_2)_2PbI_3$ ($FAPbI_3$) are studied by first-principles calculations. For comparison, the cation-doped tetragonal methylammonium lead iodine $CH_3NH_3PbI_3$ ($MAPbI_3$) are also considered. The calculated formation energies reveal that the Sn atom is easier to dope in the tetragonal $MAPbI_3$/$FAPbI_3$ structure due to the small formation energy of about 0.3 eV. Besides, the band gap of Sn-doped $MAPbI_3$/$FAPbI_3$ is 1.30/1.40 eV, which is considerably smaller than the un-doped tetragonal $MAPbI_3$/$FAPbI_3$. More importantly, compare with the un-doped tetragonal $MAPbI_3$/$FAPbI_3$, the Sn-doped $MAPbI_3$ and $FAPbI_3$ have the larger optical absorption coefficient and theoretical maximum efficiency, especially for Sn-doped $FAPbI_3$. The lower formation energy, suitable band gap and outstanding optical absorption of the Sn-doped $FAPbI_3$ make it promising candidates for high-efficient perovskite cells.

Over the last several years, hybrid organic-inorganic perovskite solar cells have become one of the most attractive photovoltaic technologies, with easy solution fabrication and high conversion efficiencies[1–8]. The first perovskite based solar cells, made seven years ago by Japanese researchers, turned just 3.8% of the energy in sunlight into electricity[9]. After that, the efficiency of perovskite solar cells has been updated rapidly as a result of new strategies adopted in their fabrication process[10–18], including device structure, interfacial engineering, chemical compositional tuning, and crystallization kinetics control. The power conversion efficiency of perovskite solar cells can greater than 20%[18, 19], which is comparable to the commercial silicon (20%), CIGS (19.6%), GaAs (18.4%) and CdTe (19.6%) solar cells[20]. More recently, a power conversion efficiency up to 22.1% under the operational condition is achieved[21]. The power conversion efficiency of perovskite solar cells is climbing faster than that of any solar technology before them.

The outstanding light absorption is one of the indispensable conditions for the high efficiency solar cells. While, the band gap plays a vital role of light absorption. If the band gap is too small, the device will be able to collect extra current but the open-circuit voltage will be too small. However, if the band gap is too wide (>2 eV), only a small fraction of solar energy can be absorbed. Thus, an absorbing layer with a band gap of approximately 1.4–1.6 eV is preferred for solar cells developed from a single junction[22]. Perovskite materials are built by the inorganic elements lead and iodine, together with simple organic compounds. Most of previous works are mainly focused on the methylammonium lead iodide ($MAPbI_3$) perovskites, with a band gap of ~1.55 eV[23–29]. Compared with un-doped $MAPbI_3$ perovskite, Sn-doped $MAPbI_3$ perovskite have a small band gap, which can further enhance the photovoltaic performance of perovskite solar cells in the near-infrared spectrum[30, 31]. Besides, Sn-doped $MAPbI_3$ perovskite allowed tunable band gap of the perovskite absorber by varying the Sn:Pb ratio[32, 33].

Once replacing organic compound methylammonium (MA) with formamidinium (FA), a slightly larger organic molecule, the absorption spectrum of perovskite is mostly concentrated in the visible and near-infrared regime[34–36]. Especially for the tetragonal $FAPbI_3$ perovskite with a band gap of 1.43 eV, which is therefore

[1]College of Physics and Electronics Engineering & College of Chemistry and Materials Science, Hengyang Normal University, Hengyang, 421008, China. [2]Beijing Computational Science Research Center, Beijing, 100084, China. [3]Center for Green Innovation, School of Mathematics and Physics, University of Science & Technology Beijing, Beijing, 100083, China. Correspondence and requests for materials should be addressed to L.-M.L. (email: limin.liu@csrc.ac.cn)

Structure	E_f (eV)	L-$H_{defect-I}$ (Å)	L-$V_{defect-I}$ (Å)
Bi-doped MAPbI$_3$	1.31	3.10	3.29
Sn-doped MAPbI$_3$	0.28	3.13	3.21
Tl-doped MAPbI$_3$	0.88	3.19	3.28
Bi-doped FAPbI$_3$	1.36	3.21	3.12
Sn-doped FAPbI$_3$	0.29	3.23	3.12
Tl-doped FAPbI$_3$	0.84	3.33	3.16

Table 1. The formation energies and detailed defect-I bond lengths of cation-doped MAPbI$_3$/FAPbI$_3$. Where the E_f, L-$H_{defect-I}$, and L-$V_{defect-I}$ are the formation energies, the average defect-I bond lengths in the horizontal surface of defect-I octahedral structure and the average defect-I bond lengths in the vertical direction of defect-I octahedral structure, respectively.
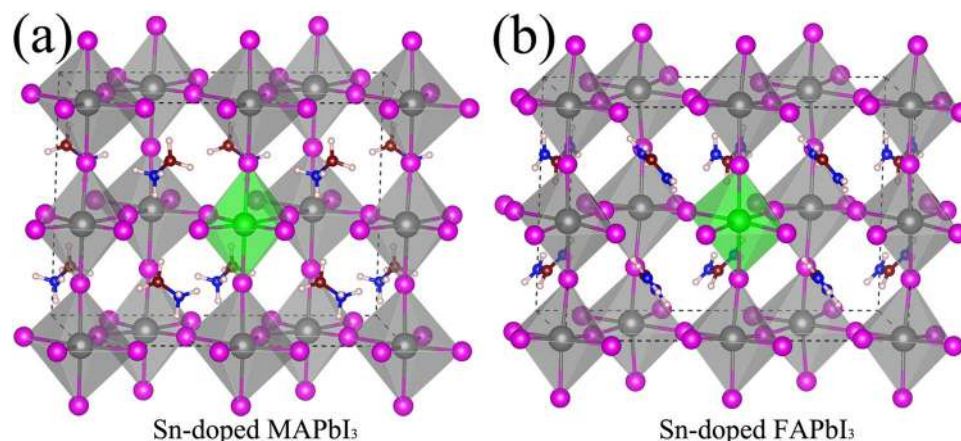

Figure 1. The relaxed atomic structures of the (**a**) Sn-doped MAPbI$_3$ and (**b**) Sn-doped FAPbI$_3$. The silver, violet, blue, brown, pink, and green balls represent Pb, I, N, C, H, and Sn atoms, respectively.

potentially superior than the trigonal FAPbI$_3$ as the light harvester[35]. Besides, the FA induced structural variability improved charge transport and red-shifted absorption in tetragonal FAPbI$_3$ structures[36]. More importantly, the highest confirmed record power conversion efficiency of PSCs is based FAPbI$_3$ perovskite[18]. We note that the FASnI$_3$ has a band gap of 1.41 eV which allows light harvesting from the near-infrared region[37]. Thus, we very curious to know the electronic structures and optical absorption properties of Sn and other cation-doped tetragonal FAPbI$_3$ perovskite.

In this work, first-principles calculations were carried to systematically examine the geometry, electronic structure, and optical properties of the cation (Bi, Sn, and Tl) doped tetragonal MAPbI$_3$/FAPbI$_3$ perovskites. The formation energies and detailed defect-I bond lengths of cation-doped MAPbI$_3$/FAPbI$_3$ are showed in the Table 1. The calculated results show that the Sn-doped defect is the common impurity in the tetragonal MAPbI$_3$/FAPbI$_3$ perovskites due to the lowest formation energy of about 0.3 eV. While, relatively higher formation energy means that both the donor defect Bi and the acceptor defect Tl are difficult to dope in MAPbI$_3$/FAPbI$_3$ perovskites. The calculated band gap of Sn-doped MAPbI$_3$/FAPbI$_3$ perovskite is 1.30/1.40 eV, respectively. The band gap of Sn-doped MAPbI$_3$/FAPbI$_3$ perovskite is smaller than that of un-doped perovskites. More importantly, the Sn-doped MAPbI$_3$ and FAPbI$_3$ perovskites have the higher specific absorption in the visible light region, especially for the Sn-doped tetragonal FAPbI$_3$ perovskite. Our electronic structures and optical properties calculations indicate that the Sn-doped tetragonal FAPbI$_3$ is a promising candidate for high-efficient perovskite cell.

Results

Before the optimization of the cation-doped perovskite structure, the lattice constants of tetragonal MAPbI$_3$ and FAPbI$_3$ supercells are fully relaxed. In the tetragonal MAPbI$_3$ supercell, the relaxed lattice constants a is 8.72 Å and c is 12.92 Å, which is in good agreement with the experimental results[32]. In addition, the relaxed lattice constants a is 9.20 Å and c is 12.54 Å in the tetragonal FAPbI$_3$ supercell. Then, we fix the lattice constants in the structural optimization of the cation-doped MAPbI$_3$/FAPbI$_3$ supercells. Considered the ion radius and the number of outside electrons, three types of atoms (Bi, Sn, and Tl) were chosen as the typical cation-doped in the MAPbI$_3$ and FAPbI$_3$. The Bi and Tl represent the donor impurity and acceptor impurity, respectively. The outsider electron number of Pb equal to the Sn atom, which is neither an acceptor impurity, nor a donor impurity. The relaxed structures of Sn doped MAPbI$_3$ and FAPbI$_3$ supercells are showed in Fig. 1(a) and (b). For the Sn-I octahedral structure in the Sn doped MAPbI$_3$, the average horizontal and vertical Sn-I bond length is 3.13 Å and 3.21 Å, respectively. The Sn-I octahedral structure in the Sn doped MAPbI$_3$ is a tensile octahedron, which vertical Sn-I bond length larger than the horizontal Sn-I bond length. However, the vertical and horizontal Sn-I bond length
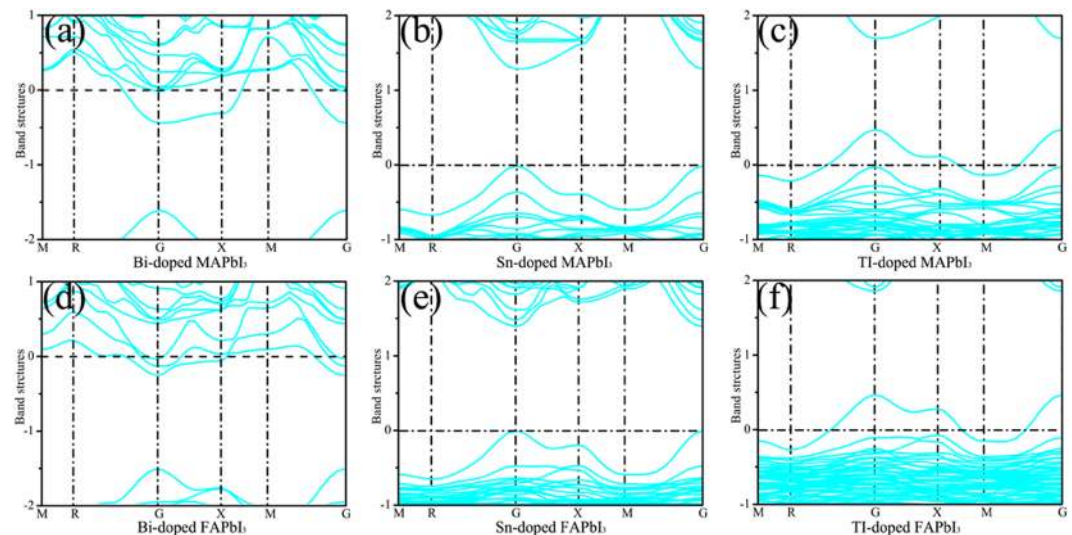
Figure 2. The band structures of the (**a**) Bi-doped MAPbI$_3$, (**b**) Sn-doped MAPbI$_3$, (**c**) TI-doped MAPbI$_3$, (**d**) Bi-doped FAPbI$_3$, (**e**) Sn-doped FAPbI$_3$, (**f**) TI-doped FAPbI$_3$.

is 3.23 Å and 3.12 Å in the Sn doped FAPbI$_3$. It means that the Sn-I octahedral structure in the Sn doped FAPbI$_3$ is a compressed octahedron.

Previous experimental and theoretical research[25] shows that the band gaps and the optical properties of MAPbI$_3$ are influenced by the cation-doping. Interesting, the Sn-doped MAPbI$_3$ possesses a favorable band gap and even greater optical absorption in the visible-light region. Therefore, it is necessary to know whether the cation-doped FAPbI$_3$ has fascinating electronic and optical properties. The band structures of the cation-doped MAPbI$_3$ and FAPbI$_3$ are calculated by density functional theory (DFT) with PBE functional. The PBE functional calculations can give reasonable electronic properties of hybrid lead iodine perovskite structure[38]. In the Bi-doped MAPbI$_3$/FAPbI$_3$, the Fermi level across the conduction band due to the donor defect Bi, as shown in the Fig. 2(a) and (d). While, the Sn-doped MAPbI$_3$/FAPbI$_3$ is the perfect semiconductor with a direct band gap at the G point. The calculated band gap of Sn-doped MAPbI$_3$ and FAPbI$_3$ is 1.30 eV and 1.40 eV, respectively. Compare with the band gap of un-doped tetragonal MAPbI$_3$ (1.50 eV) and FAPbI$_3$ (1.57 eV), the Sn-doped MAPbI$_3$ and FAPbI$_3$ have the relatively lower band gap for broader-spectrum light harvesting. For the TI-doped MAPbI$_3$/FAPbI$_3$ structure, the Fermi level is lower than the valence band maximum, as shown in the Fig. 2(c) and (f). Thus, the TI is a shallow acceptor defect in the TI-doped MAPbI$_3$/FAPbI$_3$ structure.

To get a deeper understanding the electronic properties of the cation-doped MAPbI$_3$/FAPbI$_3$, the total density of states (DOS) and partial density of states (PDOS) of Pb, I and cation defects are plotted in the Fig. 3. The partial DOS of Bi-doped MAPbI$_3$/FAPbI$_3$ shown that the electronic states near the Fermi level are mainly contributed by Bi defects, as shown in the Fig. 3(a) and (d). For the Sn-doped MAPbI$_3$/FAPbI$_3$, the valence band maximum (VBM) is mainly contributed by I atom, while the conduction band minimum (CBM) is mainly contributed by Sn and Pb atom. Besides, most PDOS of Sn defect are overlapped with the PDOS of single Pb atom becuase Sn and Pb have the same outer electron configuration. Compared with the PDOS of Pb atom, more sattes of TI in the TI-doped MAPbI$_3$/FAPbI$_3$ distributed in the high energy region, which further confirms that the TI is an acceptor defect in the doped MAPbI$_3$/FAPbI$_3$ systems.

To evaluate the optical absorption of halide perovskites, the optical absorption efficients of the Sn and TI doped MAPbI$_3$/FAPbI$_3$ perovskites are calculated and compared with the un-doped MAPbI$_3$/FAPbI$_3$ perovskites, as shown in Fig. 4. For the Sn-doped MAPbI$_3$/FAPbI$_3$, the optical absorption peak is lower than that of undoped MAPbI$_3$/FAPbI$_3$. However, the Sn-doped MAPbI$_3$ has better light absorption in the visible regions (380–780 nm), which is consistent with recent theoretical and experimental results. In contrast to the un-doped MAPbI$_3$/FAPbI$_3$, the optical absorption peak of Sn-doped MAPbI$_3$/FAPbI$_3$ exhibits a red-shift. But the optical absorption spectrum of TI-doped MAPbI$_3$/FAPbI$_3$ is lower than that of un-doped structures in most of the visible light region. At the strongest emission ares of sunlight (450–500 nm), the absorption efficient of Sn-doped FAPbI$_3$ is about in 1.5×10^6 cm^{-1}, which is 1.5 times larger than that of Sn-doped MAPbI$_3$. Considering the range of visible light accounts for the major usable portion of the full solar spectrum, the visible light absorption is critical to achieve high efficiency cells. Therefore, it is very essential to know whether the Sn-doped FAPbI$_3$ can enhance the photo-electric conversion efficiency.

In general, the effect of the optical absorption coefficient is not considered in the well-known Shockley-Queisser limit[39]. The theoretical maximum efficiency depends on the thickness of the absorber layer[40–42]. Yin et al.[26, 43] calculated the thickness-dependent maximum solar cell parameters of CH$_3$NH$_3$PbI$_3$ based on Fermi Golden rule. According to the Fermi Golden rule, the optical absorption of a photonic energy $\hbar\omega$ is directly correlated with $\frac{2\pi}{\hbar} \int |<v|\hat{H}|c>|^2 \frac{2}{8\pi^3} \delta(E_c(\vec{k})-E_v(\vec{k})-\hbar\omega)d^3k$, Where $<v|\hat{H}|c>$ is the transition matrix from states in the valence band (VB) to states in the conduction band (CB) and the integration is over the whole reciprocal space. For a real solar cell, the theoretical maximum efficiency depends on the thickness of the absorber layer[43].
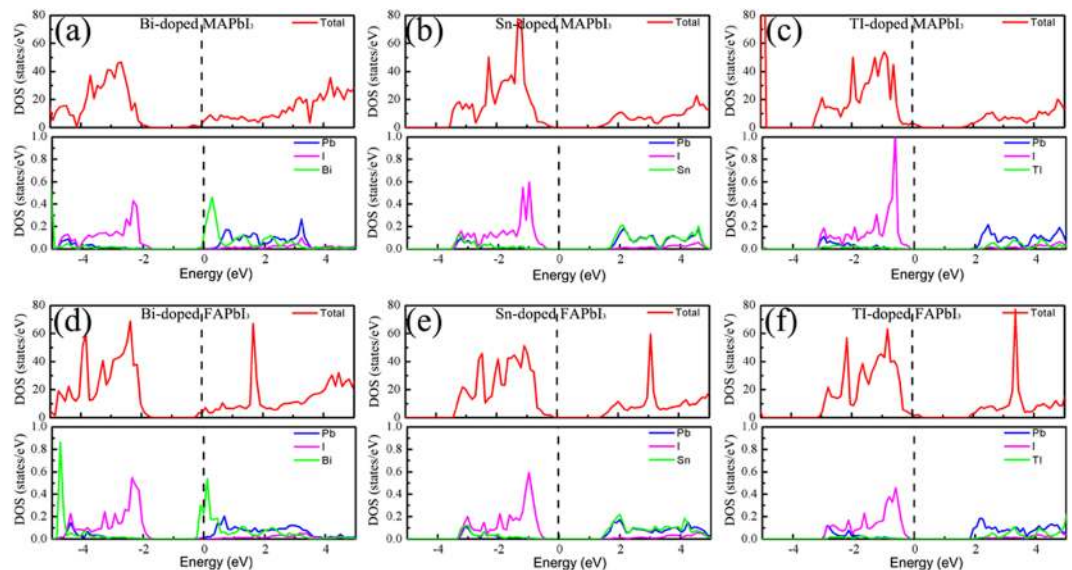
Figure 3. The total DOS and PDOS of Pb, I, and defect in the (**a**) Bi-doped $MAPbI_3$, (**b**) Sn-doped $MAPbI_3$, (**c**) Tl-doped $MAPbI_3$, (**d**) Bi-doped $FAPbI_3$, (**e**) Sn-doped $FAPbI_3$, and (**f**) Tl-doped $FAPbI_3$. In order to facilitate comparison with PDOS of defect, the PDOS of Pb and I is the average PDOS per atom. The total DOS and PDOS are shown on the upper and low panel in the subfigure. The red, blue, violet, and green lines represent the total DOS, PDOS of Pb, I, and doped cation, respectively.
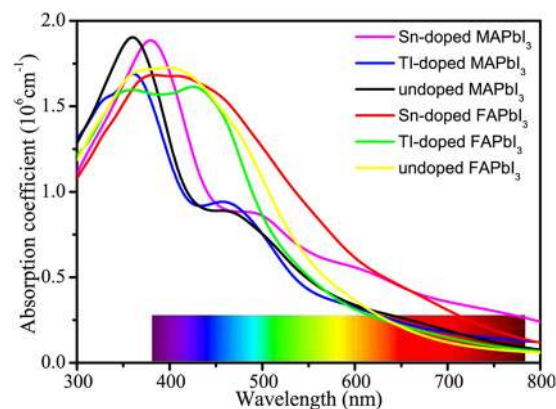
Figure 4. The calculated optical absorption spectra of the doped and undoped $MA(FA)PbI_3$. The violet, blue, black, red, green, and yellow lines represent the optical absorption spectra of the Sn-doped $MAPbI_3$, Tl-doped $MAPbI_3$, un-doped $MAPbI_3$, Sn-doped $FAPbI_3$, Tl-doped $MAPbI_3$ and un-doped $MAPbI_3$, respectively.

After taking the absorption efficient and absorber layer thickness into consideration, we have calculated the maximum efficiencies of some common light absorbers as a function of the thickness of the absorber layers, as shown in Fig. 5. With a 5 μm absorber, the maximum efficiency of Sn-doped $MAPbI_3$, Tl-doped $MAPbI_3$, un-doped $MAPbI_3$, Sn-doped $FAPbI_3$, Tl-doped $FAPbI_3$, and un-doped $FAPbI_3$ based cells is 32.4%, 25.0%, 31.3%, 32.7%, 29.3%, and 31.9%, respectively. Obviously, the Sn-doped $MAPbI_3/FAPbI_3$ perovskites exhibit much higher conversion efficiencies than un-doped $MAPbI_3/FAPbI_3$ and Tl-doped $MAPbI_3/FAPbI_3$ for any given thickness. More importantly, the Sn-doped $MAPbI_3/FAPbI_3$ perovskites are capable of achieving high efficiencies with very thin absorber layers. For example, with a 0.5 μm absorber, Sn-doped $MAPbI_3$ and Sn-doped $FAPbI_3$ based cells can have a maximum efficiency up to 23.2% and 21.9%, respectively. Considering the strong capacity of light absorption and high maximum efficiency, the Sn-doped tetragonal $FAPbI_3$ should be a more suitable candidate for the high efficiency perovskite solar cell material.

Discussions

To know the difficulty of Bi, Sn, and Tl doping in the $MAPbI_3$ and $FAPbI_3$, the formation energy, E_f, is calculated. The formation energy of the cation-doped $MAPbI_3/FAPbI_3$ is defined as follows,

$$E_f = E_{total} - E_{pure} + \mu_{Pb} - \mu_{cation} \tag{1}$$
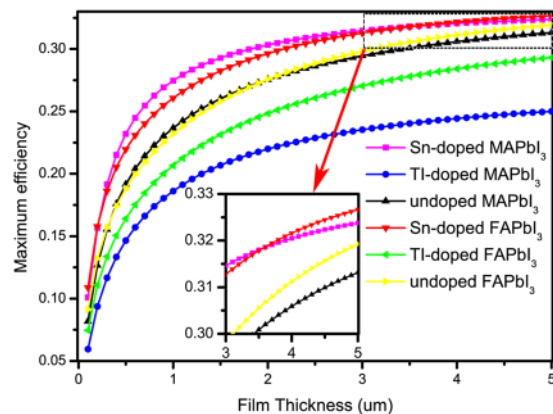
Figure 5. The calculated maximum efficiencies of the cation-doped and undoped MA(FA)PbI₃. The violet, blue, black, red, green, and yellow lines represent the maximum efficiencies of the Sn-doped MAPbI₃, Tl-doped MAPbI₃, un-doped MAPbI₃, Sn-doped FAPbI₃, Tl-doped MAPbI₃ and un-doped MAPbI₃, respectively.

where E_{total}, E_{pure}, μ_{pb} and μ_{cation} represent the total energy of the cation-doped MAPbI₃/FAPbI₃, the total energy of the primitive MAPbI₃/FAPbI₃, the chemical potential of Pb atom, and the chemical potentials of doped cations, respectively. In our calculations, the chemical potentials of the Pb and doped cations use the formation enthalpy of the corresponding most stable metal structures. The calculated formation energies are 1.31, 0.28, 0.88, 1.36, 0.29 and 0.84 eV for the Bi-doped MAPbI₃, Sn-doped MAPbI₃, Tl-doped MAPbI₃, Bi-doped FAPbI₃, Sn-doped FAPbI₃, and Tl-doped FAPbI₃ supercell, respectively. The relatively small formation energy of Sn-doped MAPbI₃/FAPbI₃ indicates that it is easy to dope Sn in the tetragonal MAPbI₃/FAPbI₃ structure. The formation energy results indicate that n-type MAPbI₃/FAPbI₃ halide perovskites (Bi-doped) are more difficult to form than p-type MAPbI₃/FAPbI₃ halide perovskites (Tl-doped).

In this work, the electronic structures and optical properties of typical cation (Bi, Sn, and Tl) doped MAPbI₃/FAPbI₃ are studied by density functional theory. The calculation results show that both the donor defect Bi and the acceptor defect Tl have the relatively high formation energies. While, the Sn defect is easy to dope in the tetragonal MAPbI₃/FAPbI₃ structure due to the small formation energy of 0.3 eV. The calculated band gap of Sn-doped MAPbI₃ and FAPbI₃ is 1.30 eV and 1.40 eV, respectively. The optical absorption effients of Sn-doped MAPbI₃/FAPbI₃ are higher than that of un-doped MAPbI₃/FAPbI₃ within the visible light range. More importantly, the Sn-doped MAPbI₃/FAPbI₃ have relatively high theoretical maximum efficiency, especially for the Sn-doped FAPbI₃. The lower formation energy, suitable band gap and outstanding optical absorption of the Sn-doped FAPbI₃, enable it has great potential applications for the high-efficient perovskite cells.

Method

The first-principles structure, energy and optical absorption calculations were performed by the Vienna Ab Initio Simulation Package (VASP)[44, 45]. Projector augmented-wave (PAW) pseudopotentials[46] were used to account electron-ion interactions. The generalized gradient approximation (GGA) with the PBE functional[47] was used to treat the exchange-correlation interaction between electrons. In order to get the appropriate doping concentration, $2 \times 1 \times 1$ MAPbI₃ and FAPbI₃ supercells are used in our calculation. The energy cutoff was set to 500 eV and a $5 \times 7 \times 7$ Monkhorst-Pack scheme was used to sample Brillouin zone[48]. The full geometry optimizations are carried out with the convergence thresholds of 10^{-4} eV and 1×10^{-2} eV/Å for total energy and ionic force, respectively. It is well-known that vdW interactions are crucial in the determination of the equilibrium configurations in the hybrid structure. Thus, the DFT-D3 approach was used to take the effect of the vdW interaction[49].

It is well known that the PBE functional always underestimated the band gap of semiconductors. Besides, the spin-orbit coupling (SOC) also results in much reduced band gaps in hybrid lead iodine perovskite structure. In the previous DFT calculation, both the hybrid HSE06 functional and spin-orbit coupling effects are considered to calculated the electronic properties of hybrid lead iodine perovskite structure. Their calculated results show that the band gap of cubic MAPbI₃ is 1.60 eV with PBE functional, while the band gap of PBE + SOC and PBE + HSE + SOC is 0.49 eV and 1.53 eV[38]. It is noted that the band gaps obtained by PBE without including SOC is quite close experimental value of 1.55 eV[9]. Thus, the PBE functional could give the reasonable band gaps for hybrid lead iodine perovskites. In addition, the calculated optical of cation-doped MAPbI₃/FAPbI₃ with PBE functional also should show the right trend.

References

1. McGehee, M. D. Perovskite solar cells: Continuing to soar. *Nat. Mater.* **13**, 845–846, doi:10.1038/nmat4050 (2014).
2. Zhou, H. *et al*. Interface engineering of highly efficient p erovskite solar cells. *Science* **345**, 542–546, doi:10.1126/science.1254050 (2014).
3. Kamat, P. V. Back to the Photovoltaic Future with Perovskites. *J. Phys. Chem. Lett.* **6**, 4874–4875, doi:10.1021/acs.jpclett.5b02524 (2015).
4. Miyasaka, T. Perovskite Photovoltaics: Rare Functions of Organo Lead Halide in Solar Cells and Optoelectronic Devices. *Chem. Lett.* **44**, 720–729, doi:10.1246/cl.150175 (2015).

5. Berry, J. *et al.* Hybrid Organic–Inorganic Perovskites (HOIPs): Opportunities and Challenges. *Adv. Mater.* **27**, 5102–5112, doi:10.1002/adma.201502294 (2015).
6. Boix, P. P., Agarwala, S., Koh, T. M., Mathews, N. & Mhaisalkar, S. G. Perovskite Solar Cells: Beyond Methylammonium Lead Iodide. *J. Phys. Chem. Lett.* **6**, 898–907, doi:10.1021/jz502547f (2015).
7. Williams, S. T., Rajagopal, A., Chueh, C. C. & Jen, A. K. Current Challenges and Prospective Research for Upscaling Hybrid Perovskite Photovoltaics. *J. Phys. Chem. Lett.* **7**, 811–819, doi:10.1021/acs.jpclett.5b02651 (2016).
8. Brenner, T. M., Egger, D. A., Kronik, L., Hodes, G. & Cahen, D. Hybrid organic—inorganic perovskites: low-cost semiconductors with intriguing charge-transport properties. *Nat. Rev. Mater.* **1**, 15007, doi:10.1038/natrevmats.2015.7 (2016).
9. Kojima, A., Teshima, K., Shirai, Y. & Miyasaka, T. Organometal Halide Perovskites as Visible-Light Sensitizers for Photovoltaic Cells. *J. Am. Chem. Soc.* **131**, 6050–6051, doi:10.1021/ja809598r (2009).
10. Burschka, J. *et al.* Tris(2-(1H-pyrazol-1-yl)pyridine)cobalt(III) as p-Type Dopant for Organic Semiconductors and Its Application in Highly Efficient Solid-State Dye-Sensitized Solar Cells. *J. Am. Chem. Soc.* **133**, 18042–18045, doi:10.1021/ja207367t (2011).
11. Im, J.-H., Lee, C.-R., Lee, J.-W., Park, S.-W. & Park, N.-G. 6.5% efficient perovskite quantum-dot-sensitized solar cell. *Nanoscale* **3**, 4088–4093, doi:10.1039/C1NR10867K (2011).
12. Kim, H.-S. *et al.* Lead Iodide Perovskite Sensitized All-Solid-State Submicron Thin Film Mesoscopic Solar Cell with Efficiency Exceeding 9%. *Sci. Rep.* **2**, 591, doi:10.1038/srep00591 (2012).
13. Stranks, S. D. *et al.* Electron-Hole Diffusion Lengths Exceeding 1 Micrometer in an Organometal Trihalide Perovskite Absorber. *Science* **342**, 341–344, doi:10.1126/science.1243982 (2013).
14. Xing, G. *et al.* Long-Range Balanced Electron- and Hole-Transport Lengths in Organic-Inorganic CH3NH3PbI3. *Science* **342**, 344–347, doi:10.1126/science.1243167 (2013).
15. Qin, P. *et al.* Inorganic hole conductor-based lead halide perovskite solar cells with 12.4% conversion efficiency. *Nat. Commun.* **5**, 3834, doi:10.1038/ncomms4834 (2014).
16. Jeon, N. J. *et al.* o-Methoxy Substituents in Spiro-OMeTAD for Efficient Inorganic–Organic Hybrid Perovskite Solar Cells. *J. Am. Chem. Soc.* **136**, 7837–7840, doi:10.1021/ja502824c (2014).
17. Zhou, H. *et al.* Interface engineering of highly efficient perovskite solar cells. *Science* **345**, 542–546, doi:10.1126/science.1254050 (2014).
18. Woon Seok, Y. *et al.* High-p erformance photovoltaic perovskite layers fabricated through intramolecular exchange. *Science* **348**, 1234–1237, doi:10.1126/science.aaa9272 (2015).
19. Saliba, M. *et al.* Cesium-containing triple cation perovskite solar cells: improved stability, reproducibility and high efficiency. *Energ. Environ. Sci.* **9**, 1989–1997, doi:10.1039/C5EE03874J (2016).
20. Green, M. A., Emery, K., Hishikawa, Y., Warta, W. & Dunlop, E. D. Solar cell efficiency tables. *Prog. Photovolt.: Res. Appl.* **22**, 701–710, doi:10.1002/pip.2525 (2014).
21. Zhou, Y. & Zhu, K. Perovskite Solar Cells Shine in the "Valley of the Sun". *ACS Energy Lett.* **1**, 64–67, doi:10.1021/acsenergylett.6b00069 (2016).
22. Yusoff, A. R. & Nazeeruddin, M. K. Organohalide Lead Perovskites for Photovoltaic Applications. *J. Phys. Chem. Lett.* **7**, 851–866, doi:10.1021/acs.jpclett.5b02893 (2016).
23. Agiorgousis, M. L., Sun, Y. Y., Zeng, H. & Zhang, S. Strong covalency-induced recombination centers in perovskite solar cell material CH3NH3PbI3. *J. Am. Chem. Soc.* **136**, 14570–14575, doi:10.1021/ja5079305 (2014).
24. Geng, W., Zhang, L., Zhang, Y.-N., Lau, W.-M. & Liu, L.-M. First-Principles Study of Lead Iodide Perovskite Tetragonal and Orthorhombic Phases for Photovoltaics. *J. Phys. Chem. C* **118**, 19565–19571, doi:10.1021/jp504951h (2014).
25. Shi, T., Yin, W.-J. & Yan, Y. Predictions for p-Type CH3NH3PbI3Perovskites. *J. Phys. Chem. C* **118**, 25350–25354, doi:10.1021/jp508328u (2014).
26. Yin, W.-J., Yang, J.-H., Kang, J., Yan, Y. & Wei, S.-H. Halide perovskite materials for solar cells: a theoretical review. *J. Mater. Chem. A* **3**, 8926–8942, doi:10.1039/c4ta05033a (2015).
27. Zhang, L. & Sit, P. H. L. Ab Initio Study of Interaction of Water, Hydroxyl Radicals, and Hydroxide Ions with CH3NH3PbI3and CH3NH3PbBr3Surfaces. *J. Phys. Chem. C* **119**, 22370–22378, doi:10.1021/acs.jpcc.5b07000 (2015).
28. Tong, C.-J. *et al.* Uncovering the Veil of the Degradation in Perovskite CH3NH3PbI3 upon Humidity Exposure: A First-Principles Study. *J. Phys. Chem. Lett.* **6**, 3289–3295, doi:10.1021/acs.jpclett.5b01544 (2015).
29. Hao, F., Stoumpos, C. C., Chang, R. P. & Kanatzidis, M. G. Anomalous band gap behavior in mixed Sn and Pb perovskites enables broadening of absorption spectrum in solar cells. *J. Am. Chem. Soc.* **136**, 8094–8099, doi:10.1021/ja5033259 (2014).
30. Ogomi, Y. *et al.* CH3NH3SnxPb(1-x)I3 Perovskite Solar Cells Covering up to 1060 nm. *J. Phys. Chem. Lett.* **5**, 1004–1011, doi:10.1021/jz5002117 (2014).
31. Shen, Q. *et al.* Optical absorption, charge separation and recombination dynamics in Sn/Pb cocktail perovskite solar cells and their relationships to photovoltaic performances. *J. Mater. Chem. A* **3**, 9308–9316, doi:10.1039/C5TA01246E (2015).
32. Feng, H. J., Paudel, T. R., Tsymbal, E. Y. & Zeng, X. C. Tunable Optical Properties and Charge Separation in CH3NH3Sn(x)Pb(1-x)I3/TiO2-Based Planar Perovskites Cells. *J. Am. Chem. Soc.* **137**, 8227–8236, doi:10.1021/jacs.5b04015 (2015).
33. Mosconi, E., Umari, P. & De Angelis, F. Electronic and optical properties of mixed Sn–Pb organohalide perovskites: a first principles investigation. *J. Mater. Chem. A* **3**, 9208–9215, doi:10.1039/c4ta06230b (2015).
34. Eperon, G. E. *et al.* Formamidinium lead trihalide: a broadly tunable perovskite for efficient planar heterojunction solar cells. *Energ. Environ. Sci.* **7**, 982–988, doi:10.1039/C3EE43822H (2014).
35. Pang, S. *et al.* NH2CH=NH2PbI3: An Alternative Organolead Iodide Perovskite Sensitizer for Mesoscopic Solar Cells. *Chem. Mater.* **26**, 1485–1491, doi:10.1021/cm404006p (2014).
36. Amat, A. *et al.* Cation-Induced Band-Gap Tuning in Organohalide Perovskites: Interplay of Spin–Orbit Coupling and Octahedra Tilting. *Nano Lett.* **14**, 3608–3616, doi:10.1021/nl5012992 (2014).
37. Koh, T. M. *et al.* Formamidinium tin-based perovskite with low Eg for photovoltaic applications. *J. Mater. Chem. A* **3**, 14996–15000, doi:10.1039/C5TA00190K (2015).
38. Kim, J., Lee, S.-C., Lee, S.-H. & Hong, K.-H. Importance of Orbital Interactions in Determining Electronic Band Structures of Organo-Lead Iodide. *J. Phys. Chem. C* **119**, 4627–4634, doi:10.1021/jp5126365 (2015).
39. Shockley, W. & Queisser, H. J. Detailed Balance Limit of Efficiency of p-n Junction Solar Cells. *J. Appl. Phys.* **32**, 510–519, doi:10.1063/1.1736034 (1961).
40. Yu, L. & Zunger, A. Identification of Potential Photovoltaic Absorbers Based on First-Principles Spectroscopic Screening of Materials. *Phys. Rev. Lett.* **108**, 068701, doi:10.1103/PhysRevLett.108.068701 (2012).
41. Yu, L., Kokenyesi, R. S., Keszler, D. A. & Zunger, A. Inverse Design of High Absorption Thin-Film Photovoltaic Materials. *Adv. Energy Mater.* **3**, 43–48, doi:10.1002/aenm.201200538 (2013).
42. Tang, Z.-K., Zhu, Y.-N., Xu, Z.-F. & Liu, L.-M. Effect of water on the effective Goldschmidt tolerance factor and photoelectric conversion efficiency of organic-inorganic perovskite: insights from first-principles calculations. *Phys. Chem. Chem. Phys.* **19**, 14955–14960, doi:10.1039/C7CP02659E (2017).
43. Yin, W.-J., Shi, T. & Yan, Y. Unique Properties of Halide Perovskites as Possible Origins of the Superior Solar Cell Performance. *Adv. Mater.* **26**, 4653–4658, doi:10.1002/adma.201306281 (2014).
44. Kresse, G. & Furthmüller, J. Efficient iterative schemes for ab initio total-energy calculations using a plane-wave basis set. *Phys. Rev. B* **54**, 11169–11186, doi:10.1103/PhysRevB.54.11169 (1996).

45. Kresse, G. & Furthmüller, J. Efficiency of ab-initio total energy calculations for metals and semiconductors using a plane-wave basis set. *Comput. Mater. Sci.* **6**, 15, doi:10.1016/0927-0256(96)00008-0 (1996).
46. Kresse, G. & Joubert, D. From ultrasoft pseudopotentials to the projector augmented-wave method. *Phys. Rev. B* **59**, 1758, doi:10.1103/PhysRevB.59.1758 (1999).
47. Perdew, J. P., Burke, K. & Ernzerhof, M. Generalized Gradient Approximation Made Simple. *Phys. Rev. Lett.* **77**, 3865, doi:10.1103/PhysRevLett.77.3865 (1996).
48. Monkhorst, H. J. & Pack, J. D. Special points for Brillouin-zone integrations. *Phys. Rev. B* **13**, 5188–5192, doi:10.1103/PhysRevB.13.5188 (1976).
49. Grimme, S., Antony, J., Ehrlich, S. & Krieg, H. A consistent and accurate ab initio parametrization of density functional dispersion correction (DFT-D) for the 94 elements H-Pu. *J. Chem. Phys.* **132**, 154104, doi:10.1063/1.3382344 (2010).

Acknowledgements

Author Contributions

The work was initiated by Z.T. and L.L., with research ideas supplying by Z.T., and L.L. during the work progresses. The simulation was performed by Z.T. The data analyses were performed by Z.T., Z.X., D.Z., S.H. and M.L. This manuscript was written by Z.T., and L.L. The results and their interpretation were collectively discussed by all authors.

Additional Information

Competing Interests: The authors declare that they have no competing interests.

Publisher's note: Springer Nature remains neutral with regard to jurisdictional claims in published maps and institutional affiliations.